Naval Research Laboratory

Washington, DC 20375-5320

NRL/FR/7130-00-9946

Generalized Hydrodynamics with Viscoplasticity for Channeling in Saturated Sand

WILLIAM G. SZYMCZAK

Physical Acoustics Branch
Acoustics Division

JOEL C.W. ROGERS

Department of Applied Mathematics and Physics
Polytechnic University
Brooklyn, NY

June 22, 2000

REPORT DOCUMENTATION PAGE

Form Approved
OMB No. 0704-0188

1. AGENCY USE ONLY (*Leave Blank*)	2. REPORT DATE	3. REPORT TYPE AND DATES COVERED
	June 22, 2000	Interim — Oct. 1997 to present

4. TITLE AND SUBTITLE

Generalized Hydrodynamics With Viscoplasticity for Channeling in Saturated Sand

5. FUNDING NUMBERS

PE - 62315N
TA - 01526
WU - 71-7456

6. AUTHOR(S)

William G. Szymczak and Joel C.W. Rogers*

7. PERFORMING ORGANIZATION NAME(S) AND ADDRESS(ES)

Naval Research Laboratory
Washington, DC 20375-5320

8. PERFORMING ORGANIZATION REPORT NUMBER

NRL/FR/7130--00-9946

9. SPONSORING/MONITORING AGENCY NAME(S) AND ADDRESS(ES)

Monitoring Agnecy:
Naval Surface Warfare Center
Indian Head, MD

Sponsoring Agency:
Office of Naval Research
800 North Quincy Street
Arlington, VA 22217-5660

10. SPONSORING/MONITORING AGENCY REPORT NUMBER

11. SUPPLEMENTARY NOTES

*Department of Applied Mathematics and Physics, Polytechnic University,
Brooklyn, NY 11201

12a. DISTRIBUTION/AVAILABILITY STATEMENT

Approved for public release; distribution is unlimited.

12b. DISTRIBUTION CODE

13. ABSTRACT (*Maximum 200 words*)

In this report we review the "Generalized Formulation of Hydrodynamics" for a single incompressible species with free surfaces and consider methods to extend this formulation to the multiple species case. Constraints on the species volume fractions are imposed using successive redistributions. Formulations that include material strength and viscosity are described. A non-Newtonian viscous model, which approximates a Bingham plastic model, is described and implemented. Benchmark computations are performed to assess the accuracy of the computational model. Numerical simulations of explosive channeling in sand under a layer of water are presented with some comparisons to experimental data.

14. SUBJECT TERMS

Bingham plastic
Saturated sand
Free surface
Channeling
Explosion bubble
Non-Newtonian viscosity

15. NUMBER OF PAGES

30

16. PRICE CODE

17. SECURITY CLASSIFICATION OF REPORT	18. SECURITY CLASSIFICATION OF THIS PAGE	19. SECURITY CLASSIFICATION OF ABSTRACT	20. LIMITATION OF ABSTRACT
UNCLASSIFIED	UNCLASSIFIED	UNCLASSIFIED	UL

NSN 7540-01-280-5500

Standard Form 298 (Rev. 2-89)
Prescribed by ANSI Std 239-18
298-102

CONTENTS

INTRODUCTION 1

MULTIPLE SPECIES FORMULATIONS 3

Two Species Model 3
General *m*-Species Case 5

VISCOSITY AND PLASTIC DEFORMATION 6

Material Models 6
Viscoplastic Flow in a Circular Tube 8

GENERALIZED HYDRODYNAMICS ALGORITHM FOR NON-NEWTONIAN FLUIDS 9

NUMERICAL RESULTS 12

Computations of Flow in a Circular Tube 12
Slug Flow 13
Explosive Channeling Results 15

SUMMARY AND CONCLUSIONS 24

ACKNOWLEDGMENTS 25

REFERENCES 25

GENERALIZED HYDRODYNAMICS WITH VISCOPLASTICITY FOR CHANNELING IN SATURATED SAND

INTRODUCTION

An important issue in littoral warfare is the clearance of obstacles and mines to enable a beach landing. One possible solution to this problem is to use explosives to form craters and channels in the sandy soil [1, 2]. The simulation of this phenomenon offers a great challenge to computational models, not only because of violent free-surface motions but also due to the complex interaction of the water with the sand bottom. This report describes an attempt to model this problem, using a viscoplastic description for saturated sand, within a previously developed method for simulating violent free-surface motions.

In a single-charge underwater explosion, a gas bubble forms immediately after the detonation shock wave. This bubble is initially composed of high-pressure gas that causes the bubble to grow spherically [3]. As the bubble radius increases, its pressure drops (adiabatically). When the bubble pressure drops below the ambient pressure, its radius will begin to decelerate and the bubble will eventually attain a maximum volume. At this time, the bubble pressure is at a minimum and the bubble will begin to collapse. Except at very great depths or in cases when any boundaries are sufficiently far from the charge and gravity is absent, the bubble will usually not remain spherical during its collapse. Indeed, at relatively shallow depths or cases when a boundary is near the charge, the bubble will lose its spherical shape before it attains its maximum size. Bubble jetting usually occurs during the collapse phase. This can be predicted either by theory [4] or by direct simulation. For example, in a shallow depth explosion (which does not vent), a plume of water is ejected upward above the bubble as the bubble attains its maximum volume. At the same time, another jet of water flows downward from the plume through the bubble as it begins its collapse [4, 5, 6].

Consider the case when the charge is placed in shallow water above a sandy bottom. A crater can be expected to form as the high-pressure gas causes the bubble to expand, pushing the water upward and saturated sand downward. If the bubble does not vent, the downward moving jet will impact the bottom of the sand crater and cause further excavation. At later times the sediment from the sand-water mixture refills part of the crater. The dynamics of the sand-water slurry during the violent collapse of the bubble and subsequent re-expansion are not well understood.

As can be expected, the dynamics and the final crater size will depend on the properties of the saturated sand. This dependence was noted in Ref. 7, Ch. 6 in which empirical laws were given for crater radius as a function of the charge depth (height of water). Due to the variance in the types of bottoms, the empirical laws for crater radius were stated to have a general prediction accuracy of $\pm 30\%$. It was also reported in Ref. 7 that the crater depths have an even greater variance with soil type. The most dramatic example of this dependence is the experimental results using similar charge configurations at different sites as indicated in Refs. 8 and 9. For example, explosions in shallow water conducted at Port Wakefield, Australia [8], always produced craters or channels in the sand. However, shallow water explosions over the sand in the Eglin Air Force Base Test Pond [9] caused the sand to be raised, forming a berm.

Manuscript approved December 16, 1999.

In previous work [5, 6, 10-13], the authors and colleagues have developed a computational capability for free surface flows in an incompressible fluid based on a generalized hydrodynamics model. The code BUB2D has been used to simulate two-dimensional (2-D) or axially symmetric problems, and BUB3D simulates fully three-dimensional (3-D) flows. The generalized model provides a method for density and momentum redistribution, in such a way that the density constraint on the incompressible liquid is satisfied, and energy is nonincreasing. The energy property of this method makes it unique among volume of fluid (VOF) type procedures, which usually simply truncate any excesses in density without any guarantee that mass is conserved or energy is nonincreasing [14, 15]. In addition to the improved stability provided by the unique redistribution method, stable and accurate procedures are employed for the other steps in the solution process. For example, a second-order Godunov method is used for the treatment of the nonlinear convective terms, and an approximate pressure projection method is employed for the determination of the pressure, so that the flow is divergence free in the liquid region.

While these codes have been applied to many flow situations, the most relevant to surf-zone explosive cratering problems are the examples of shallow depth explosions in a single incompressible species (water) [5, 6]. The presence of saturated sand complicates the situation, primarily due to its dual dynamical properties. For example, if a bed of sand is shaken (or driven with enough force), it becomes fluidized [16-18]. However, sand (particularly, wet sand) can obviously behave as a solid, a fact that anyone who has built a sandcastle can attest to. This dual property suggests that some form of "plasticity" is required for an appropriate model.

Traditional continuum models for granular flows are usually based on the Mohr-Coulomb criterion for failure. This criterion states that yielding will occur on a plane element when

$$|S| = c + T\tan(\phi),$$

where S is the shear stress, c is the cohesion, T is the normal stress, and ϕ is the internal angle of friction for the granular material. Constitutive laws, which have incorporated this criterion, have been presented in, for example, Refs. 19 to 21. Alternately, a Drucker-Prager discontinuity condition was used in place of the Mohr-Coulomb criterion in Refs. 22 and 23. This condition was claimed to have computational advantages over the Mohr-Coulomb criterion, while producing similar results [22].

For the present study, however, we have chosen a Bingham plastic model for the saturated sand. This model provides a simple viscoplastic description, consisting of only a yield stress and a viscosity during yielding [24]. It is typically used to describe the rheology in fluids with a large amount of suspended solids [25] and has been used in the description of debris flow [26]. Furthermore, for channel-flow problems, models using the Mohr-Coulomb criterion have been shown to exhibit a plug region in the center of the channel, similar to that of a Bingham fluid [19]. More realistic descriptions of rate dependent stress models can be easily incorporated into our numerical algorithm, but this report only discusses the capabilities and limitations of applying the Bingham model.

This report begins by providing a brief outline of the generalized hydrodynamics model and its extension (in particular, the redistribution phase) to multiple species. A description of material models, including plasticity, is given in the next section. Particular emphasis is placed on the use of non-Newtonian viscosity, in particular, a Bingham plastic model for the saturated sand. The details of implementing an approximation to the Bingham plastic model within the context of generalized hydrodynamics are also presented. Validations are shown for benchmark problems, including comparisons to an analytic solution of flow in a circular cylinder. Finally, a comparison is made from videos taken from an experiment and computations using various values for the yield stress within the Bingham model for sand.

MULTIPLE SPECIES FORMULATIONS

In this section, a description of our generalized hydrodynamics model is presented together with the modifications required for the treatment of multiple incompressible species. We start with the simple inviscid case; the formulation and implementation of viscosity are described in detail in the succeeding sections.

Two Species Model

For simplicity, first consider the two-species case where, for example, the species are saturated sand and water. For the remainder of this paper we will refer to "saturated sand" as simply "sand." Let ρ be the mixture density,

$$\rho = \rho_s \phi_s + \rho_w \phi_w, \tag{1}$$

where ρ_s is the density of sand, ρ_w is the density of water, and $\phi_s \geq 0$, $\phi_w \geq 0$ are the *volume fractions* of sand and water, respectively. For an inviscid fluid mixture in which the two species move with a common velocity (without any material strength), the Conservation of Momentum equation is

$$(\rho \mathbf{u})_t + \nabla \bullet (\rho \mathbf{u}\mathbf{u}) = -\nabla P - \rho g \mathbf{k}, \tag{2}$$

where $\mathbf{u} = (u, v, w)$ is the fluid (mixture) velocity, P is the pressure, g is the acceleration due to gravity, and $\mathbf{k}$ is the unit vector in the direction opposite to the gravity. (In the actual formulation of the Generalized Formulation of Hydrodynamics considered here, the pressure gradient does not explicitly appear in the momentum conservation. Instead, it is added in implicitly as a Lagrange multiplier used to satisfy constraints on the density and the effect of these constraints on the conservation of mass equation. For a more detailed discussion on this, see Refs. 10 to 13.) The Conservation of Mass may be expressed as conservation of each species volume; namely,

$$(\phi_s)_t + \nabla \bullet (\phi_s \mathbf{u}) = 0, \tag{3}$$

$$(\phi_w)_t + \nabla \bullet (\phi_w \mathbf{u}) = 0. \tag{4}$$

Equations (3) and (4) are solved with the constraints:

$$\phi_w \leq 1, \tag{5}$$

$$\phi_s \leq 1, \tag{6}$$

$$\phi_s + \phi_w \leq 1. \tag{7}$$

Note, the only actual constraint is Eq. (7) since Eq. (7) together with the non-negativity of the volume fractions yields Eqs. (5) and (6). Also, the non-negativity of these variables is preserved by the solution of Eqs. (3) and (4), so that $\phi \geq 0$ need not be explicitly imposed as a constraint. Note, that Eqs. (3) and (4) yield

$$\nabla \bullet \mathbf{u} = 0 \qquad \text{when } \phi_w + \phi_s = 1, \tag{8}$$

which is the usual divergence free condition for incompressible flow. Also Eqs. (1), (3), and (4) yield

$$\rho_t + \nabla \bullet (\rho \mathbf{u}) = 0, \tag{9}$$

which is the usual mass conservation equation.

This constrained system of conservation laws can be approximated using the Generalized Formulation of Hydrodynamics for Multiple Species. For single species, this formulation was first proposed in Ref. 10. This formulation may be stated as an algorithm that advances the flow $(\rho^n, \mathbf{u}^n)$ at time t^n to the flow $(\rho^{n+1}, \mathbf{u}^{n+1})$ at time $t^{n+1} = t^n + \tau$.

The first step is to approximate the solution to Eqs. (2) to (4) without the constraints Eqs. (5) to (8) and without the pressure term in the momentum equations. This solution can be obtained by approximating the coupled Eqs. (2) and (9) (which are the same as for a single incompressible species) and including either Eqs. (3) or (4), (say Eq. (3)). We denote this flow as $(\tilde{\rho}, \tilde{\mathbf{u}})$ and let $\tilde{\phi}_s$ denote the intermediate "sand" volume fraction. Then

$$\tilde{\phi}_w = \frac{\tilde{\rho} - \rho_s \tilde{\phi}_s}{\rho_w}.$$

follows from Eq. (1).

We seek a redistribution which satisfies the following three criteria:

1. The species volume fractions satisfy the constraints Eqs. (5) to (7).
2. The total volumes of each species are conserved.
3. The total energy is nonincreasing.

For a single species, this is accomplished by setting

$$\rho^{n+1} = \tilde{\rho} + \nabla^2 H \tag{10}$$

and

$$\rho^{n+1} \bar{\mathbf{u}} = \tilde{\rho} \tilde{\mathbf{u}} + \nabla^2 (H \bar{\mathbf{u}}), \tag{11}$$

where $H \geq 0$ is the solution of the "obstacle problem"

$$\nabla^2 H = \begin{cases} \rho_w - \tilde{\rho}, & \text{if} \quad H > 0 \\ 0, & \text{if} \quad H = 0 \end{cases}. \tag{12}$$

The redistributed velocity $\bar{\mathbf{u}}$ defined in Eq. (11) requires the solution of a linear elliptic system of equations. For multiple species, the Eqs. (10) and (11) will still be used (together with Eq. (2)) so that criterion C will be satisfied. The redistribution function H must be constructed differently, depending on the redistribution of the individual species volume fractions.

The strategy for redistribution will be denoted as the "successive constraint" approach. For this procedure, the redistribution function H is defined by

$$H = \rho_s H_s + \rho_w H_w, \tag{13}$$

where H_s and H_w are successively defined using

$$\nabla^2 H_s = \begin{cases} 1-\tilde{\phi}_s, & if \quad H_s > 0 \\ 0, & if \quad H_s = 0 \end{cases} \tag{14}$$

and

$$\nabla^2 H_w = \begin{cases} 1-\tilde{\phi}_w - \phi_s^{n+1}, & if \quad H_w > 0 \\ 0, & if \quad H_w = 0 \end{cases}, \tag{15}$$

with the redistributed volume fractions given by

$$\phi_s^{n+1} = \tilde{\phi}_s + \nabla^2 H_s \tag{16}$$

and

$$\phi_w^{n+1} = \tilde{\phi}_w + \nabla^2 H_w. \tag{17}$$

Applying the maximum principle to Eq. (14) yields $\nabla^2 H_s \le 1-\tilde{\phi}_s$. This, together with Eq. (16), implies that $\phi_s^{n+1} \le 1$. Similarly, Eqs. (15) and (17) ensure that $\phi_w^{n+1} + \phi_s^{n+1} \le 1$. Finally, Eqs. (1), (13), (16), and (17) yield

$$\rho^{n+1} = \rho_s \phi_s^{n+1} + \rho_w \phi_w^{n+1} = \tilde{\rho} + \nabla^2 H, \tag{18}$$

which is consistent with Eq. (10).

The final step carries the solution from $\left(\rho^{n+1}, \bar{\mathbf{u}}\right)$ to $\left(\rho^{n+1}, \mathbf{u}^{n+1}\right)$ so that the constraint Eq. (8) is satisfied. This is done by projecting the velocity onto its divergence free subspace in the domain where $\phi_w + \phi_s = 1$. This projection involves the addition of the gradient of the pressure (used here as a Lagrange multiplier) to the momentum. That is

$$\rho^{n+1}\mathbf{u}^{n+1} = \rho^{n+1}\bar{\mathbf{u}} - \tau\nabla P\,, \tag{19}$$

where P solves the equation

$$\tau\nabla \bullet \frac{1}{\rho^{n+1}}\nabla P = \nabla \bullet \bar{\mathbf{u}} \qquad \text{in } D^{n+1}, \tag{20}$$

where D^{n+1} is the "incompressible" region where $\phi_w + \phi_s = 1$. In practice, this region is defined to be the region where $\phi_w + \phi_s \ge 1-\varepsilon$ for some prescribed value of ε. Outside of this region, the pressure is assumed to be uniform within each component. For example, in the "air" region, the pressure is set to the ambient pressure P_A. Inside a bubble, the pressure is determined using an adiabatic law. Note, that Eqs. (19) and (20) yield

$$\nabla \bullet \mathbf{u}^{n+1} = \nabla \bullet \bar{\mathbf{u}} - \tau\nabla \bullet \frac{1}{\rho^{n+1}}\nabla P = 0 \qquad \text{in } D^{n+1}. \tag{21}$$

General *m*-Species Case

In the case when there are m species and

$$\rho = \sum_{i=1}^{m} \rho_i \phi_i , \tag{22}$$

the transport species equations are

$$(\phi_i)_t + \nabla \bullet (\phi_i \mathbf{u}) = 0 , \qquad \text{for } i = 1, ..., m. \tag{23}$$

The successive constraint procedure for imposing $\sum_{i=1}^{m} \phi_i \le 1$ is accomplished by setting

$$\phi_i^{n+1} = \tilde{\phi}_i + \nabla^2 H_i , \tag{24}$$

where H_i solves

$$\nabla^2 H_i = \begin{cases} 1 - \tilde{\phi}_i - \sum_{j=1}^{i-1} \phi_j^{n+1}, & if \quad H_i > 0 \\ 0, & if \quad H_i = 0 \end{cases}, \qquad \text{for } i = 1, ..., m. \tag{25}$$

Then

$$\rho^{n+1} = \sum_{i=1}^{m} \rho_i \phi_i^{n+1} = \tilde{\rho} + \sum_{i=1}^{m} \rho_i \nabla^2 H_i = \tilde{\rho} + \nabla^2 H , \tag{26}$$

where

$$H = \sum_{i=1}^{m} \rho_i H_i . \tag{27}$$

As with the two-species formulation, Eq. (11) is used for the momentum redistribution with H given by Eq. (27), and energy cannot increase. The pressure projection is performed exactly as before, following Eqs. (19) to (21).

VISCOSITY AND PLASTIC DEFORMATION

In this section, we discuss some material models including both Newtonian and non-Newtonian viscosity, and elastic-plastic deformation. The implementation of an "exponential" non-Newtonian viscous model, which can closely approximate a Bingham plastic model, is discussed in some detail.

Material Models

Consider the momentum equation with the inclusion of viscous and/or material stresses,

$$(\rho \mathbf{u})_t + \nabla \bullet (\rho \mathbf{u}\mathbf{u}) = -\nabla \bullet \sigma - \rho g \mathbf{k} , \tag{28}$$

with

$$\sigma = P\mathbf{I} - \mathbf{T} , \tag{29}$$

where P is the pressure, $\mathbf{I}$ is the 3×3 identity matrix (tensor), and $\mathbf{T}$ is the *stress tensor*. In the case when $\mathbf{T} = \mathbf{T}(\Delta)$, where

$$\Delta \equiv \nabla \mathbf{u} + (\nabla \mathbf{u})^* - \tfrac{2}{3}(\nabla \bullet \mathbf{u})\mathbf{I}, \tag{30}$$

is the *rate of deformation tensor,* then $\mathbf{T}$ is referred to as a *viscous stress tensor*. Note, that for incompressible flow, the divergence of the velocity is zero. However, we include it here in the definition of Δ since our model includes compressible (nonliquid) regions. For a Newtonian fluid, the dependence of the stress on the rate of deformation tensor is linear, (cf. [24])

$$\mathbf{T} = \mu(\phi)\Delta, \tag{31}$$

where the coefficient $\mu = \mu(\phi)$ may depend on the volume fractions of the fluids.

Elastic-Plastic Materials

For the material stress, one possibility is a linear elastic-plastic model in the form:

$$\mathbf{T} = \begin{cases} \mathbf{C}(\mathbf{E} - \Pi) & \text{if } \|\mathbf{E} - \Pi\| < E_Y \\ \mathbf{A}(\mathbf{E} - \Pi) \pm \hat{\tau} & \text{if } \|\mathbf{E} - \Pi\| = E_Y \end{cases}, \tag{32}$$

where $\mathbf{C}$ and $\mathbf{A}$ are linear operators (tensors) relating the strain $\mathbf{E}$ to the stress, Π is the *permanent plastic deformation*, E_Y is the *yield strain*, $\hat{\tau}$ is the *yield stress*, and $\|\bullet\|$ is an appropriate norm acting on the strain tensor. The strain tensor satisfies the system of equations (this represents an approximation to the strain)

$$\frac{\partial \mathbf{E}}{\partial t} + \mathbf{u} \bullet \nabla \mathbf{E} = \Delta, \tag{33}$$

and Π is evolved using the equation

$$\frac{\partial \Pi}{\partial t} + \mathbf{u} \bullet \nabla \Pi = \begin{cases} \dfrac{\partial \mathbf{E}}{\partial t} + \mathbf{u} \bullet \nabla \mathbf{E} & \text{if } \|\mathbf{E} - \Pi\| = E_Y \\ 0 & \text{if } \|\mathbf{E} - \Pi\| < E_Y \end{cases}. \tag{34}$$

The Eqs. (33) and (34) each represent an additional six equations (three in 2-D or axi-symmetry) for the tensor components of $\mathbf{E}$ and Π. Constitutive laws of the form Eq. (32) depend only on the strain of the material and are often referred to as "rate-independent."

Viscous Models

Alternatively, it may be more appropriate to use a rate-dependent material description. A nonlinear rate dependence can be incorporated directly (without the need for introducing extra variables as with Eq. (33)) into the momentum equations using a non-Newtonian fluid approximation. One non-Newtonian fluid that includes plastic behavior is the Bingham Model [24, 25, 27]. This model uses a discontinuous stress-strain rate law and may be described using (cf. Ref. 24, p. 103)

$$\mathbf{T} = \left\{ \mu_0 + \frac{\hat{\tau}}{\sqrt{\frac{1}{2}(\Delta : \Delta)}} \right\} \Delta, \quad \text{if } \tfrac{1}{2}(\mathbf{T} : \mathbf{T}) \geq \hat{\tau}^2, \tag{35a}$$

$$\Delta = 0, \quad \text{if } \tfrac{1}{2}(\mathbf{T} : \mathbf{T}) < \hat{\tau}^2. \tag{35b}$$

According to Bird et al. (Ref. 25, p. 227) "The viscoplastic models are particularly useful for describing liquids with large amounts of suspended solids," and may be appropriate for the limiting case of saturated sand. An approximation to the discontinuous stress described in Eq. (35) has been recently proposed by Papanastasiou and Boudouvis in Ref. 28. This exponential model has the form

$$\mathbf{T} = \left\{ \mu_0 + \frac{\hat{\tau}\left[1 - \exp\left(-\alpha\sqrt{\frac{1}{2}(\Delta : \Delta)}\right)\right]}{\sqrt{\frac{1}{2}(\Delta : \Delta)}} \right\} \Delta. \tag{36}$$

A comparison of using Eq. (36) with various α compared to Eq. (35) is shown in Fig. 1. For $\alpha = 0$ this model reverts to Newtonian viscosity. It approaches the Bingham model Eq. (35) as $\alpha \to \infty$.

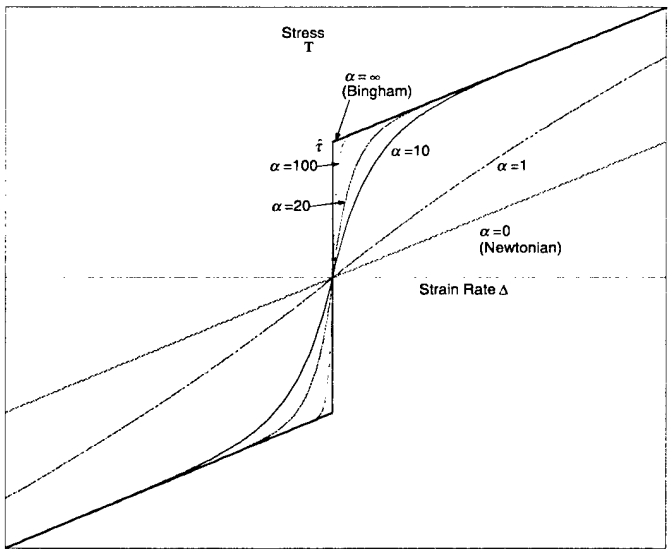

Fig. 1 — Stress–strain rate graphs using the Papanastasiou model Eq. (36)

Viscoplastic Flow in a Circular Tube

Consider the steady-state flow of a viscous fluid, through a circular tube of radius R and length L, with pressures P_0 and P_L specified at the ends of the tube. In this case, the radial velocity component is zero and the axial velocity $v = v(r)$ depends only on the radial location r. Both the deformation and stress tensors have a single non-zero component. By considering the conservation of momentum Eqs. (28) to (29) including the hydrostatic pressure due to gravity into P_L and integrating in space along both the axial and radial component, yields

$$\mathbf{T} = \frac{P_L - P_0}{2L} r. \tag{37}$$

When $P_L \geq P_0$, it follows that $v'(r) \equiv \frac{\partial v}{\partial r} \geq 0$. After applying Eq. (36), we obtain

$$\mathbf{T} = \mu_0 v' + \hat{\tau}(1 - e^{-\alpha v'}). \tag{38}$$

Using a no-slip boundary condition $v(R) = 0$, the solution to Eq. (37) to (38) may be expressed as

$$v(r) = -\int_r^R g^{-1}\left(\frac{P_L - P_0}{2L} s\right) ds, \tag{39}$$

where g^{-1} denotes the inverse of g with $g(y) \equiv \mu_0 y + \hat{\tau}(1 - e^{-\alpha y})$. In the case, when $\alpha = 0$, $g^{-1}(y) = \frac{y}{\mu_0}$ and the usual Newtonian viscous parabolic flow follows directly from Eq. (39):

$$v(r) = -\left(\frac{P_L - P_0}{4\mu_0 L}\right) R^2 \left(1 - \left(\frac{r}{R}\right)^2\right). \tag{40}$$

For the Bingham model, the velocity is given by (see Ref. 24)

$$v(r) = \begin{cases} -\left(\frac{P_L - P_0}{4\mu_0 L}\right) R^2 \left(1 - \frac{r_0}{R}\right)^2 & r \leq r_0 \\ -\left(\frac{P_L - P_0}{4\mu_0 L}\right) R^2 \left(1 - \frac{r}{R}\right)\left(1 + \frac{r}{R} - \frac{2r_0}{R}\right) & r \geq r_0 \end{cases}, \tag{41}$$

where $r_0 = \frac{2L\hat{\tau}}{P_L - P_0}$.

Figure 2 shows solutions for v corresponding to different values of the parameter α. The solutions for $0 < \alpha < \infty$ were computed using Newton's method to determine g^{-1}, with trapezoid rule approximation of the integral Eq. (39). The maximum relative error in velocity between the Bingham model and the exponential model Eq. (36) is approximately $2/\alpha$ for $\alpha \geq 10$. Note the "plug flow" behavior of the Bingham model for $r \leq r_0$.

GENERALIZED HYDRODYNAMICS ALGORITHM FOR NON-NEWTONIAN FLUIDS

Here we describe a temporal discretization for the momentum Eq. (28) in the case of a non-Newtonian fluid. That is, we will consider Eqs. (28) and (29) with $\mathbf{T}$ defined in Eq. (36). For our multiple species case, the material coefficients μ_0 and $\hat{\tau}$ will depend on the volume fractions. To clarify the notation for the functional dependence of $\mathbf{T}$ on $\mathbf{u}$ and $\boldsymbol{\phi}$, we express

$$\mathbf{T}(\phi, \mathbf{u}) = f(\phi, \Delta(\mathbf{u}))\Delta(\mathbf{u}), \tag{42}$$

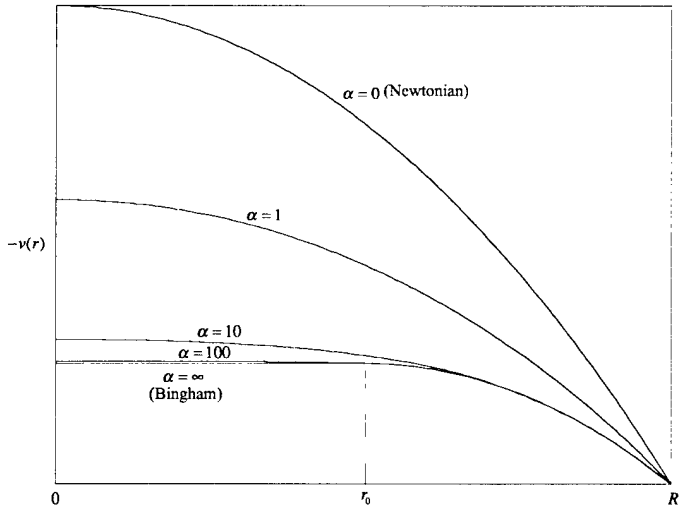

Fig. 2 — Velocity profiles for model flows in a circular tube

where Δ is a linear operator on **u** defined in Eq. (30) and

$$f(\phi,\Delta)=\mu_0(\phi)+\frac{\hat{\tau}(\phi)\left[1-\exp\left(-\alpha\sqrt{\tfrac{1}{2}(\Delta:\Delta)}\right)\right]}{\sqrt{\tfrac{1}{2}(\Delta:\Delta)}}. \tag{43a}$$

An exponential dependence was used for the viscous and yield stress terms for the saturated sand, based on an empirical data fit for slurry flows [29]. For example, the dependence of the yield stress on the volume fraction of saturated sand is given by

$$\hat{\tau}(\phi)=\hat{\tau}(\phi_s)=\hat{\tau}\frac{exp(\kappa_\tau\phi_s)-1}{exp(\kappa_\tau)-1}, \tag{43b}$$

where κ_τ is an empirically determined constant, and (with a slight misuse of notation) associates the constant $\hat{\tau}$ appearing in the right-hand side of Eq. (43b) with $\hat{\tau}(1)$. The same functional form is used for $\mu_0(\phi)$.

The first step of the algorithm is the explicit *convection* step. This represents an approximation to the solution without including any of the terms on the right-hand side of the momentum Eq. (28). That is

$$\tilde{\rho}\tilde{\mathbf{u}}=(\rho\mathbf{u})^n-\tau\nabla\bullet(\rho\mathbf{u}\mathbf{u})^{n+1/2}, \tag{44a}$$

$$\tilde{\phi}_i=\phi_i^n-\tau\nabla\bullet(\phi_i\mathbf{u})^{n+1/2}, \tag{44b}$$

for $i = 1, \ldots, m$, and

$$\tilde{\rho}=\sum_{i=1}^{m}\rho_i\tilde{\phi}_i. \tag{44c}$$

In Eq. (44) the superscript $n+1/2$ indicates an approximation at the half-time step. This step is implemented using a predictor-corrector Godunov scheme (see Refs. 11 and 13 for details). While the

corrector step of this scheme Eq. (44) ignores the pressure, gravity and stresses in Eq. (28), these terms are included in the predictor step.

The redistribution step can now proceed exactly as before using Eqs. (10) and (11), with H defined using the successive constraint approach Eqs. (24) to (27). As before, the redistributed velocity is denoted $\bar{\mathbf{u}}$, and the redistributed density and volume fractions are simply ρ^{n+1}, and ϕ_i^{n+1}, $i = 1, \ldots, m$, respectively.

The viscous stresses are included in the *diffusion* step as the solution $\mathbf{u}^*$ to

$$\rho^{n+1}\mathbf{u}^* - \rho^n\mathbf{u}^n = -\tau\nabla\bullet(\rho\mathbf{u}\mathbf{u})^{n+1/2} + \nabla^2(H\bar{\mathbf{u}}) - \tau\rho^{n+1/2}g\mathbf{k} - \tau\nabla P^{n-1/2} + \tau\nabla\bullet\left((1-\theta)\mathbf{T}(\phi^{n+1/2},\mathbf{u}^n) + \theta\mathbf{T}(\phi^{n+1/2},\mathbf{u}^*)\right), \tag{45}$$

where $\rho^{n+1/2} = \dfrac{\rho^{n+1}+\rho^n}{2}$ (similarly for ϕ), and θ is a temporal discretization parameter for the diffusion term $0 \le \theta \le 1$. The value $\theta = 0$ corresponds to the explicit "Euler" method, $\theta = 1/2$ to the second-order trapezoid rule, and $\theta = 1$ to the fully implicit "Backward Euler" method. Note that except for the lagging of the pressure gradient and the inclusion of the momentum redistribution term, this equation is a second-order temporal (trapezoid rule) discretization of the momentum Eq. (28) in the case when $\theta = 1/2$. Using Eqs. (44) and (11) with Eq. (45), we obtain

$$\rho^{n+1}\mathbf{u}^* - \rho^{n+1}\hat{\mathbf{u}} = \tau\theta\nabla\bullet\mathbf{T}(\phi^{n+1/2},\mathbf{u}^*) - \tau\theta\nabla\bullet\mathbf{T}(\phi^{n+1/2},\mathbf{u}^n), \tag{46}$$

where

$$\rho^{n+1}\hat{\mathbf{u}} = \rho^{n+1}\bar{\mathbf{u}} - \tau\rho^{n+1/2}g\mathbf{k} - \tau\nabla P^{n-1/2} + \tau\nabla\bullet\mathbf{T}(\phi^{n+1/2},\mathbf{u}^n). \tag{47}$$

Subtracting $\rho^{n+1}\mathbf{u}^n$ and setting $\delta = \mathbf{u}^* - \mathbf{u}^n$, it follows from Eqs. (42) and (46) that

$$\rho^{n+1}\delta - \tau\theta\nabla\bullet\left(f(\phi^{n+1/2},\Delta(\delta+\mathbf{u}^n))\Delta(\delta)\right) = \rho^{n+1}\left(\hat{\mathbf{u}}-\mathbf{u}^n\right) + \tau\theta\nabla\bullet\left(\left\{f(\phi^{n+1/2},\Delta(\delta+\mathbf{u}^n)) - f(\phi^{n+1/2},\Delta(\mathbf{u}^n))\right\}\Delta(\mathbf{u}^n)\right). \tag{48}$$

This represents a nonlinear equation for $\boldsymbol{\delta}$. Since the derivative of f becomes singular as $\alpha\to\infty$ and $|\Delta|\to 0$, instead of solving Eq. (48) using Newton's method, the iteration scheme

$$\rho^{n+1}\delta^{[k]} - \tau\theta\nabla\bullet\left(f(\phi^{n+1/2},\Delta(\delta^{[k-1]}+\mathbf{u}^n))\Delta(\delta^{[k]})\right) = \rho^{n+1}\left(\hat{\mathbf{u}}-\mathbf{u}^n\right) + \tau\theta\nabla\bullet\left(\left\{f(\phi^{n+1/2},\Delta(\delta^{[k-1]}+\mathbf{u}^n)) - f(\phi^{n+1/2},\Delta(\mathbf{u}^n))\right\}\Delta(\mathbf{u}^n)\right) \tag{49}$$

is used with $\delta^{[0]} = \hat{\mathbf{u}} - \mathbf{u}^n$ for $k \ge 1$. Each step of Eq. (49) corresponds to the solution of a linear system of equations. Upon discretization in space, the linear matrix corresponding to the left-hand side of Eq. (49) is symmetric and positive definite. If f is independent of $\boldsymbol{\Delta}$, the last term on the right-hand side of Eq. (49) vanishes and the iterations converge in a single step (the equation is linear in this case). In the special case when $f \equiv 0$, Eq. (49) represents a trivial identity with $k = 0$. Due to the "stiff" nature of the linear equations when $\hat{\tau}\alpha$ is large, the value $\theta = 1$ was used for all the computations presented here.

The final step is the pressure projection. To keep this part of the algorithm analogous to the inviscid version, the lagged pressure gradient must be added back to the momentum. That is, the projected momentum is

$$\rho^{n+1}\mathbf{u}^{n+1} = \rho^{n+1}\mathbf{u}^{*} + \tau\nabla P^{n-1/2} - \tau\nabla P^{n+1/2}, \tag{50}$$

where $P^{n+1/2}$ solves the equation

$$\tau\nabla \bullet \frac{1}{\rho^{n+1}}\nabla P^{n+1/2} = \nabla \bullet \bar{\mathbf{u}}^{*} \quad \text{in } D^{n+1}, \tag{51}$$

with

$$\rho^{n+1}\bar{\mathbf{u}}^{*} = \rho^{n+1}\mathbf{u}^{*} + \tau\nabla P^{n-1/2}. \tag{52}$$

In practice, Eq. (51) is not solved in "delta" form since the domain D^{n+1} and the Dirichlet values of P on the boundaries of the bubbles change with time.

NUMERICAL RESULTS

Three distinct numerical problems are considered in this section. The first is the classical problem of viscous flow in a circular tube that was described in the preceding section with exact solutions plotted in Fig. 2. The second example simulates a cylindrical "slug" of fluid, initially at rest in a larger cylindrical tank. This example demonstrates the qualitative capability of the continuous non-Newtonian model to simulate viscoplastic material strength in the fluid, thereby, allowing "sand castles" to stand. Finally, we compare experiments to simulations of explosions in saturated sand under a layer of water.

Computations of Flow in a Circular Tube

For our first example, we consider the problem of viscous flow in a circular tube (see Fig. 2). In particular, we have considered the specific problem with $R = 4$, $\frac{P_L - P_0}{2L} = 1$, $\mu_0 = 1$, and $\hat{\tau} = 2$, so that the plug-flow region for the limiting Bingham fluid model is $r \le r_0 = 2$. The convergence of the computed solutions to the "exact" solutions (using Eq. (38)) was studied by decreasing the grid spacing in the radial direction. In particular, a sequence of grids with N_r = 4, 8, 16, and 32 uniform cells were used. In each case, only four uniform cells were used to discretize the tube along its length. Initially, the velocity inside the tube was set to zero, and the solutions were marched in time to steady state, driven by the pressure boundary conditions at the tube ends.

Figure 3 shows a comparison for the Newtonian (α = 0) flow case. Even on the coarsest grid with only four cells, the maximum nodal error is only 0.1%. In this example, the solutions for all the computations are close to the exact solution.

Figure 4 shows the results for the case α = 100, which is within 1% of the solution of the limiting Bingham plastic case. In this case, the computational errors were much larger than for the Newtonian case. However, it is apparent from Fig. 4 that the solutions improve as the grid is refined.

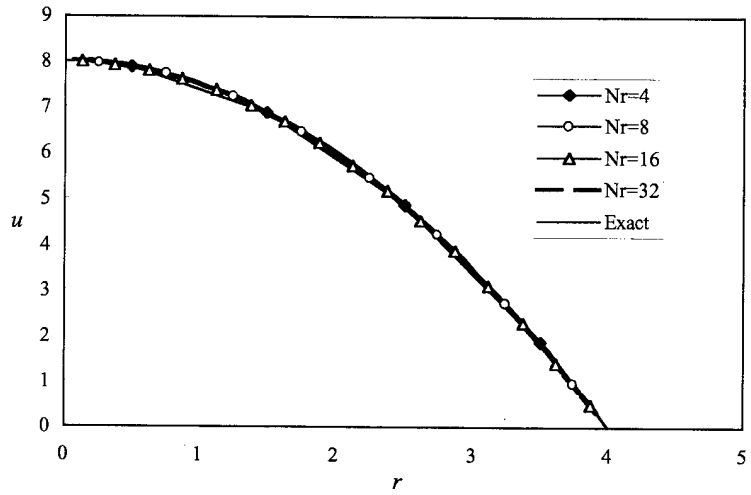

Fig. 3 — Computed and exact solution to Newtonian flow in a circular tube

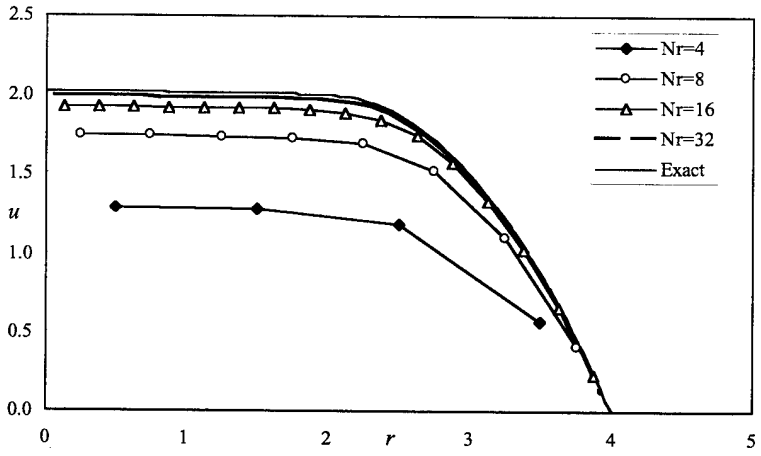

Fig. 4 — Computed and exact solutions to generalized Bingham flow ($\alpha = 100$) in a circular tube

Table 1 lists a summary of the computed maximum errors and rates of convergence. As noted in Figs. 3 and 4 above, the errors are much larger for the $\alpha = 100$ case. For the Newtonian model, the nodal rate of convergence was about 3, indicative of super-convergence at the nodal points. In general, only a second-order convergence rate could be expected. However, for the Bingham model, the rate of convergence was only about 1.5, possibly due to the discontinuity in the second derivative of the solution at the point where the flow becomes plastic.

Slug Flow

In our next example, we examine the qualitative behavior of a model of a Bingham plastic slurry. It is obvious that sand (particularly wet sand) does not flow like a Newtonian fluid and can sustain nontrivial deformations. We demonstrate numerically, how sand castles can be simulated using the Papanastasiou approximation Eq. (36) to the Bingham plastic model.

Table 1 — Errors and Rates of Convergence for Circular Tube Flow Problem

	$\alpha = 0$			$\alpha = 100$		
N_r	λ_s	Rel. Error%	Rate	λ_s	Rel. Error%	Rate
4	1.0	1.06e-1		0.4	36.26	
8	1.0	1.27e-2	3.06	0.4	13.72	1.40
16	1.0	1.63e-3	2.96	0.4	5.09	1.43
32	1.0	2.50e-4	2.70	0.4	1.76	1.53

Consider a cylindrical slug of a slurry initially at rest in a larger cylindrical tank with rigid walls in which gravity is acting. The problem has been nondimensionalized by setting $\rho_s = 1$, $g = 1$, $P_A = 1$, and $\phi_s = 1$ inside a cylinder of radius 1/4 and height 1. The boundary walls of the cylindrical tank have radius 1/2. A uniform grid of square cells of size $h = 1/32$ was used for the simulations. For comparison, we repeated the simulation for several different cases listed in Table 2.

Table 2 — Bingham Parameters for Different Slug Flow Problems

Case	μ_0	$\hat{\tau}$	α	τ
A	0	0	0	5.0e-4
B	0.01	0	0	5.0e-4
C	0	0.2	50	5.0e-4
D	0	0.2	200	5.0e-4
E	0	0.3	200	5.0e-4
F	0	0.5	200	5.0e-4
G	0	0.5	200	2.5e-4

Case A is the flow of an incompressible inviscid liquid cylinder and is included for the sake of comparison. Figure 5 displays density profiles and velocity vectors for this case at various times. The density contours are drawn at five levels $\rho = \phi_s = \{0.1, 0.3, 0.5, 0.7, 0.9\}$. To improve visualization, velocity vectors are drawn only from the centers of the lower left corner cell within each 2 by 2 block of cells. A vector is drawn whenever $\rho \geq 0.01$ to highlight spray regions. A relative scale for the length of the velocity vectors is used. The value listed below each frame next to the arrow is the maximum speed in the region where $\rho \geq 0.01$ and corresponds to the length of the adjacent arrow. The second value in parentheses is the maximum speed in the "liquid" region where $\rho \geq 0.9$. Note the "spray" region, which forms as the liquid falls after rising up the side walls. The sloshing of the liquid continues for a substantial time until numerical dissipation finally causes the liquid to come to a level rest (not shown).

Case B represents slug flow for a Newtonian viscous fluid and is displayed in Fig. 6. In this case, the rising of the liquid up the side walls is not nearly as high as the inviscid case, and no spray is formed. The convergence of this flow to the trivial steady state level solution is evidenced in the last three frames.

Cases C and D are approximations to non-Newtonian Bingham flow. The value $\hat{\tau} = 0.2$ exceeds the stress due to gravity at the top of the slug but not at the bottom. Thus, the cylindrical slug will flow similar to a stagnation flow at the bottom, while the top region will fall as a rigid plug. When the fluid at the bottom reaches the cylindrical walls, the stress is reduced below the yield stress and the fluid stops.

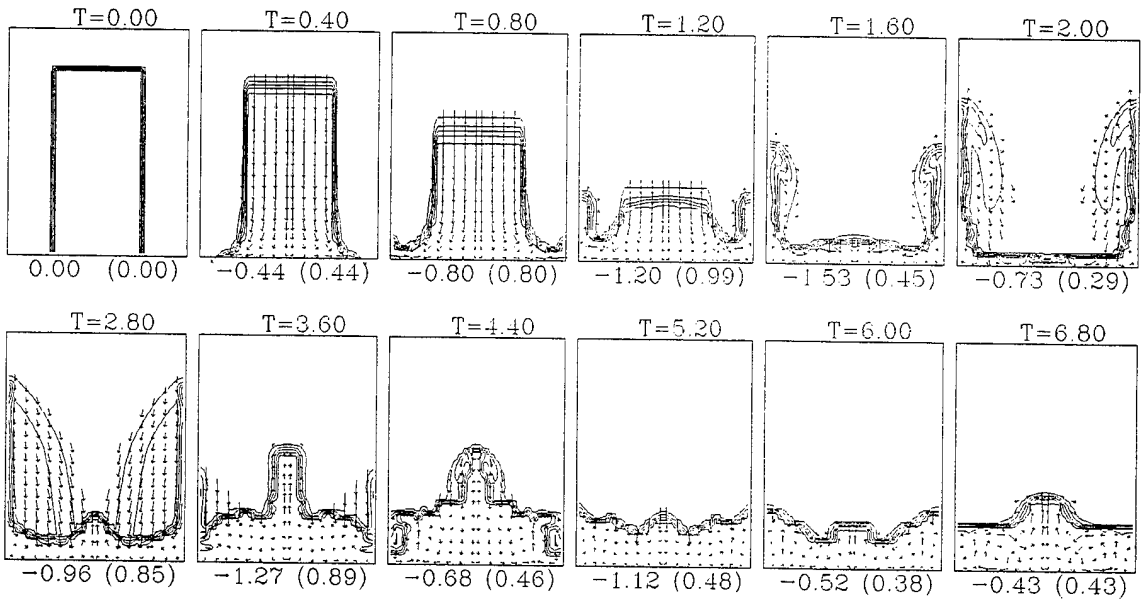

Fig. 5 — Slug flow for an inviscid incompressible liquid (Case A)

Figure 7 shows the results for the Papanastasiou approximation to Bingham flow, with the parameter $\alpha = 50$, and Fig. 8 displays the approximation with $\alpha = 200$. Note that the higher value for α causes the fluid in the region where the yield stress is exceeded to flow at an earlier time. This is due to the fact that if the yield stress is exceeded, the "effective viscosity" (the slope of the curves depicted in Fig. 1) converges to $\mu_0(=0)$ as $\alpha \to \infty$. Therefore, the region of yielding flow in Case C experiences a higher viscosity than in Case D. Note, however, that the final steady-state solutions ($T \geq 4.00$) for both cases have very similar nontrivial profiles. Next, we consider the case when the spread of the slug does not reach the wall boundary. Figure 9 displays this case and clearly demonstrates the model's ability to simulate sand castles.

Figure 10 displays a slug which behaves as a rigid body. The slight motion as indicated by a small indentation in the top of the slug and a small contour line near the bottom center are due to numerical error. Fig. 11 shows the same example computed with the time steps halved. This example indicates that while small time steps are not required for the overall stability of the algorithm, they are still needed for accuracy when the Bingham yield stress is high.

Explosive Channeling Results

The motivation for this research was the ability to predict channels and craters formed in sand from underwater explosions. A small-scale 2-D test box has been constructed at the University of Maryland to visually examine the dynamics of explosive channeling [33]. This test box (referred to as the UMD 2-D Box) is depicted with dimensions in Fig. 12. In this box, a layer of sand and water are sandwiched between a plexiglass front and aluminum plate back. The distance between the front and back plates is small with respect to the size of a free-field spherical bubble in water formed from the detonation. Therefore, neglecting viscous effects at the plate boundaries, the dynamics of the bubble, water, and sand will be primarily 2-D.

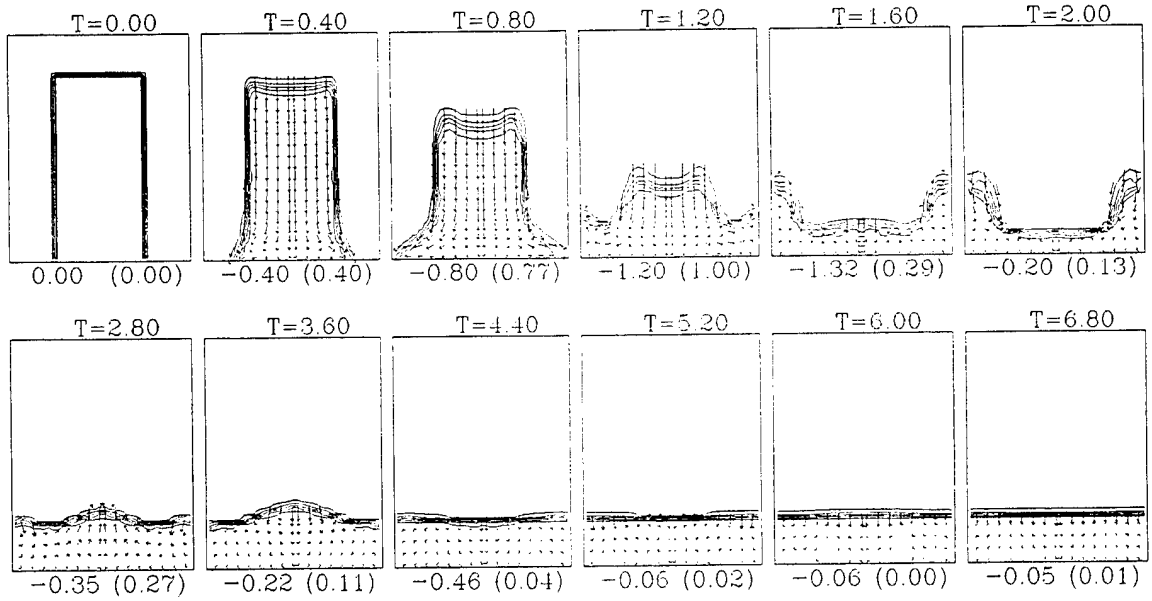

Fig. 6 — Slug flow for an viscous incompressible liquid (Case B)

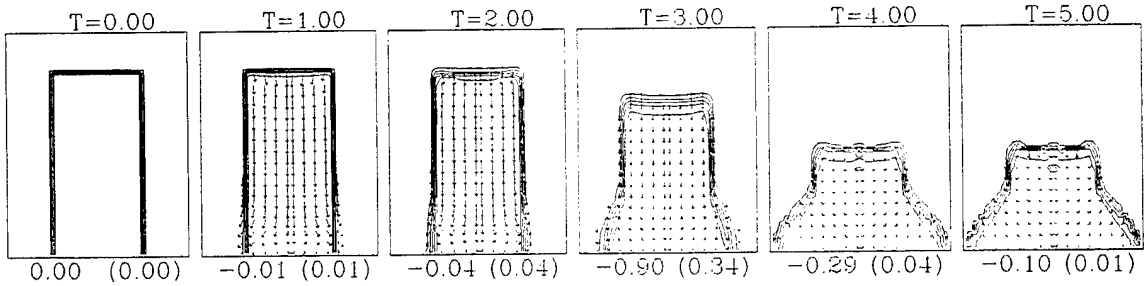

Fig. 7 — Slug flow for Case C ($\mu_0 = 0, \hat{\tau} = 0.2$, and $\alpha = 50$)

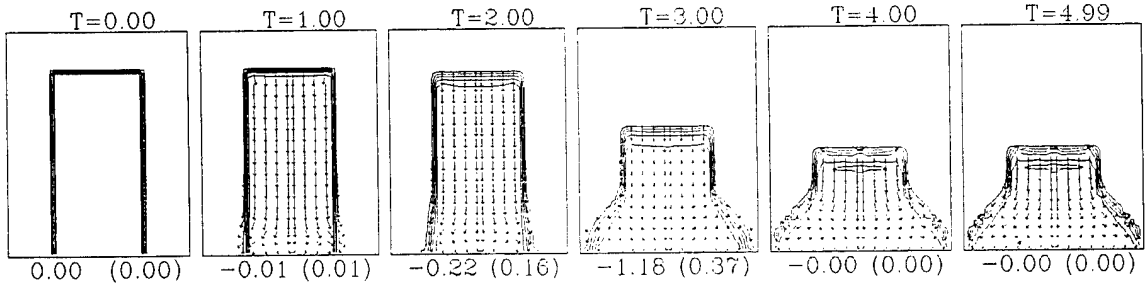

Fig. 8 — Slug flow for Case D ($\mu_0 = 0, \hat{\tau} = 0.2$, and $\alpha = 200$)

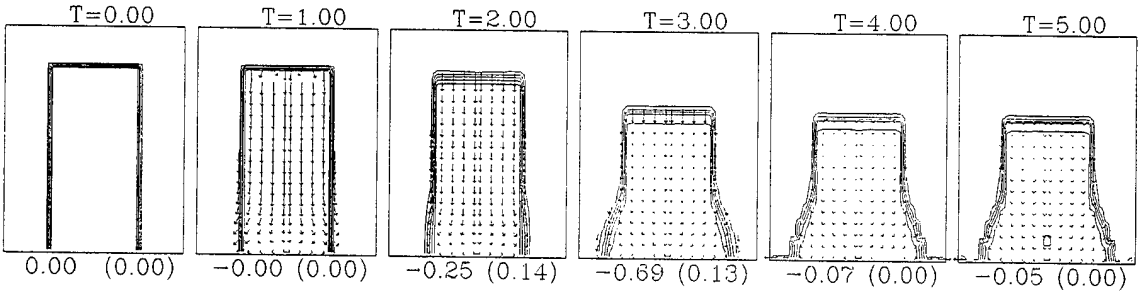

Fig. 9 — Slug flow for Case E ($\mu_0 = 0, \hat{\tau} = 0.3$, and $\alpha = 200$)

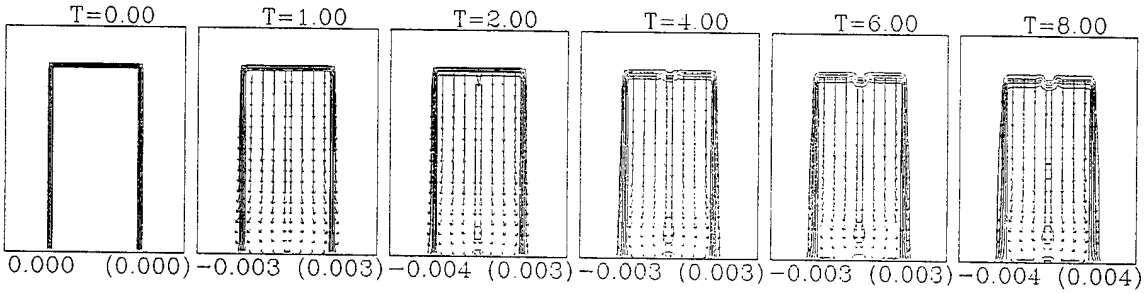

Fig. 10 — Slug flow for Case F ($\mu_0 = 0, \hat{\tau} = 0.5, \alpha = 200$, and $\tau = 5e-4$)

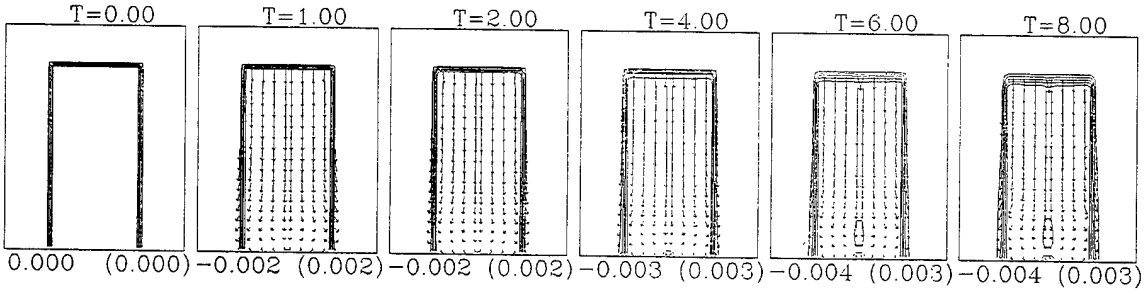

Fig. 11 — Slug flow for Case G ($\mu_0 = 0, \hat{\tau} = 0.5, \alpha = 200$, and $\tau = 2.5e-4$)

The charges used in the experiments were RP-80 detonators containing 0.203 grams of explosive. The experiments were photographed using a digital camera which recorded 500 frames per second at a resolution of 512 × 512 pixels and a depth of 8-bits (grayscale). (Additional details of the experimental setup and instrumentation may be found in Ref. 33.) The images shown were enhanced by first reducing noise with a Total Variation Minimization algorithm [30], followed by contrast equalization [31]. The noise reduction was sufficiently small (the variance of the image was reduced by only 2%), so that no important features were removed.

Figure 13 contains images from an experiment in which the initial height of water H_w was 2.5 in., and the depth of burial D_b was approximately 1 in. (measured from the top of the sand to the center of the charge). In these images, the sand was "striped" using dye to improve the visualization of the channel formation. Each stripe is approximately 1 in. thick. Shortly after detonation, a gas bubble forms and continues to expand until it attains it maximum size at $t = 0.008$. During the expansion, a water column

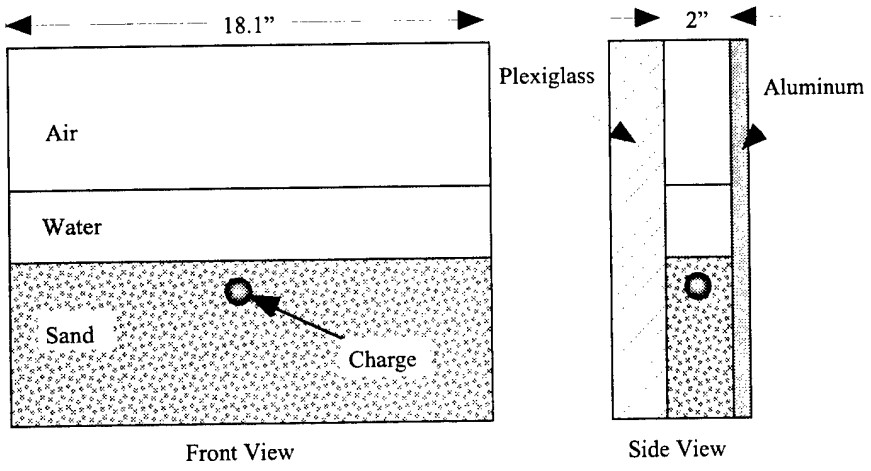

Fig. 12 — The UMD 2-D box experimental setup

(unfortunately mostly obscured by the ruler) rises above the bubble. The outline of the bubble is partially obscured by the light sand, particularly on the sides above the initial sand level. The bubble is best observed at $t = 0.010$, when it is marked by dark spots surrounded by a mixture of light sand and water. After the bubble maximum is attained, low pressure inside the bubble causes it to contract as seen in the images corresponding to times $0.010 \le t \le 0.016$. The important feature to note in these images is the formation of a downward water jet moving through the center of the bubble. This jet appears as a dark object near the top of the bubble at $t = 0.012$, which moves downward at $t = 0.014$ and $t = 0.016$. The channel walls appear to be widened after the jet impacts the bottom and flows up the sides during $0.018 \le t \le 0.100$. The sand is suspended in the slurry mixture at $t = 0.200$, and $t = 0.500$ and begins to settle out and flow back into the channel at $t = 1.000$. After $t = 1.500$, the channel reaches a steady state, where the *true crater* has been partially refilled by sediment to form a shallower *apparent crater.* The observation of "true" and "apparent" craters also appears from experiments of explosives buried in soil without a water layer, as discussed in Ref. 1. The use of dyed sand in the experiments enhances the distinction between the true and apparent craters at $t = 1.500$.

Computations were performed under the assumption that the experiment is nearly 2-D. Empirical laws are used to initialize the computation based on the theory described in Refs. 5 and 6. For a 2-D computation, the explosion is initialized as a high-pressure cylinder of gas in fluids which are initially at rest. Effects of the shock wave are neglected in this study. The bubble pressure is assumed to behave adiabatically $P_B = CV_B^{-\gamma}$; where C is a constant, V_B is the bubble volume and γ is the ratio of specific heats of the bubble gases. Following Refs. 5 and 6 and using the superscript *(2D)* to denote a 2-D value (no superscript is used for 3-D), we have

$$A_{min}^{(2D)} = q^{(2D)} M^{1/2}, \tag{53}$$

$$q^{(2D)} = \frac{2}{\sqrt{3}} q^{3/2}, \tag{54}$$

$$\alpha^{(2D)} = \alpha^{3/2}, \tag{55}$$

$$J_{\infty}^{(2D)} = \frac{2}{\sqrt{3}} J_{\infty}^{3/2}, \tag{56}$$

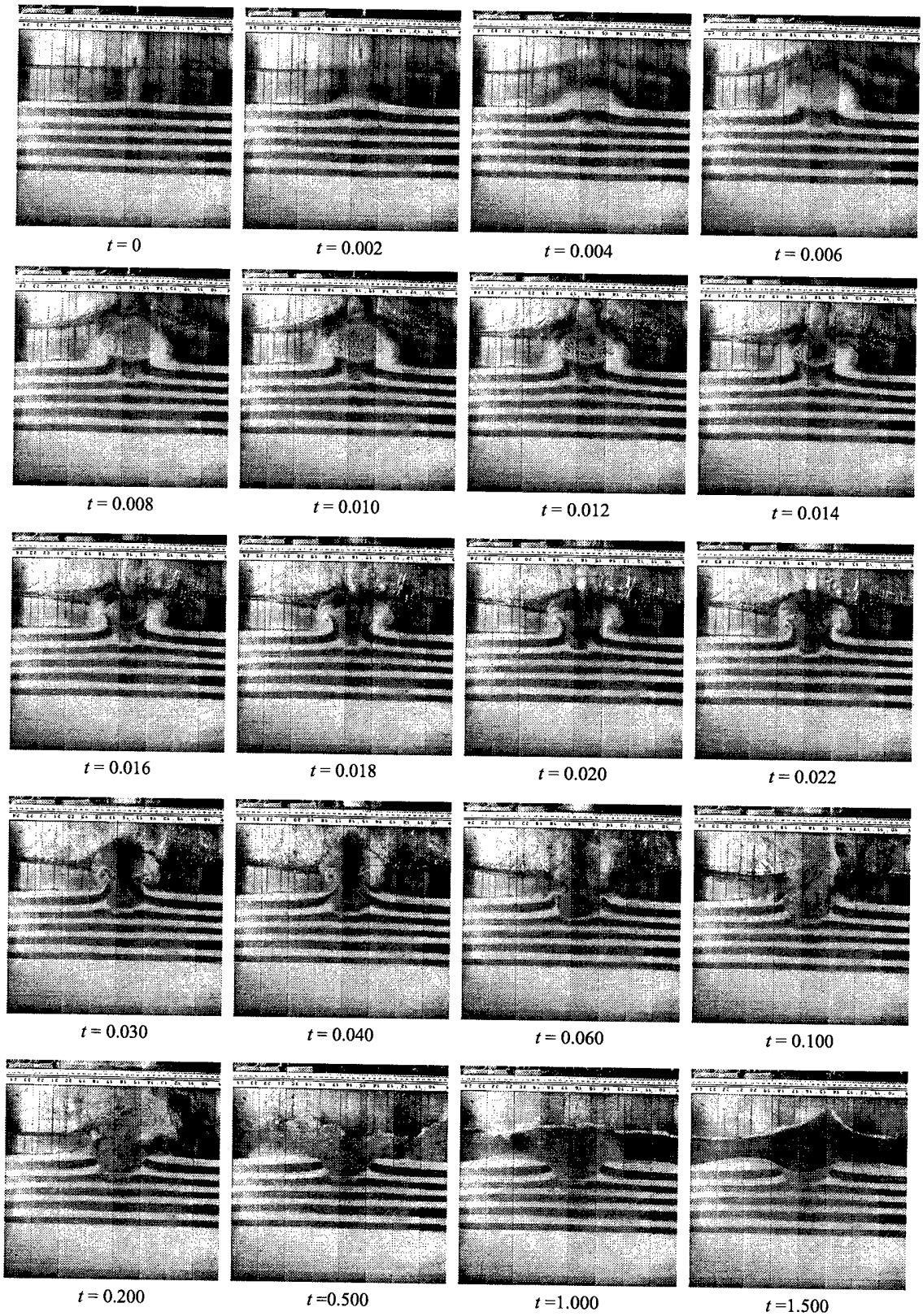

Fig. 13 — Bubble expansion and collapse from the UMD 2-D box experiment $H_w = 2.5$ in. and $D_b = 1.0$ in.

$$A_{\max}^{(2D)} = J_{\infty}^{(2D)}\left(\frac{1-(\alpha^{(2D)})^{2(1-\gamma)}}{1-(\alpha^{(2D)})^{-2\gamma}}\right)^{1/2}\frac{M^{1/2}}{P_{\infty}^{1/2}}, \tag{57}$$

$$P_B^0 = P_{\infty}(1-\gamma)\left(\frac{1-(\alpha^{(2D)})^{2}}{1-(\alpha^{(2D)})^{2(1-\gamma)}}\right), \tag{58}$$

where $A_{min}^{(2D)}$ is the initial (minimum) radius of the cylinder, $q^{(2D)}$ is the empirical *minimum radius constant* depending on the charge type, and M is the mass per unit length of the charge. The free-field maximum radius is $A_{max}^{(2D)}$ and $\alpha^{(2D)} = A_{max}^{(2D)} / A_{min}^{(2D)}$. The other empirical constant depending on the charge type is $J_{\infty}^{(2D)}$, often referred to as the *maximum radius constant*. As was discussed in detail in Ref. 5, Eq. (57) is often approximated using

$$A_{\max}^{(2D)} = J^{(2D)}\frac{M^{1/2}}{P_{\infty}^{1/2}}, \tag{59}$$

which is a valid only when the charge is very deep relative to the maximum bubble radius. Instead, we use the corrected Eq. (57), which requires the solution of a scalar nonlinear equation for the determination of $\alpha^{(2D)}$ and, hence, P_B^0. The traditional units used for underwater explosion bubbles are feet for length, pounds for charge weight, and feet of water for the pressure. The pressure at infinity P_{∞} is taken to be the hydrostatic head at the initial charge depth. For example, under ambient conditions in fresh water, we have

$$P_{\infty} = 33.9 + d, \tag{60}$$

where d is the initial depth in feet, and P_{∞} is measured in units of feet of water. Initial conditions for the computations shown here were derived from the above equations with constants $J_{\infty} = 11.0$, $q = 0.272$ and $\gamma = 1.3$. This value used for J_{∞} is approximately 30% lower than expected for RP-80 detonators. It is conjectured that the smaller than expected bubble sizes are due to either the lack of rigidity of the front and back faces of the 2-D box or the rigid body motion of the entire 2-D box during the tests. The entire box would typically "jump" about 1 in. after the charge was detonated.

Since the radius ratio $\alpha^{(2D)} = 41.6$ is large, and it is desirable to resolve the bubble at both its minimum and maximum volumes; different grids were used at different time intervals of the simulation. All grids contained a rectangular region $0 \le x \le X_R$ and $Z_B \le z \le Z_T$ of square cells of size h. This rectangle is surrounded by coarser cells that are stretched to the physical boundaries of the 2-D box. We use the convention that $x = 0$ is a symmetry line and $z = 0$ is the initial location of the air-water interface. The total number of cells in the entire domain is denoted by $N_x \times N_z$. Table 3 shows a description of the grids and time intervals in which they were used. Grid 1 is used to resolve the very small bubble at early times until it grows to approximately five times its initial radius. The flow field is then mapped onto Grid 2, such that mass and momentum are conserved and the computation is restarted. Grid 3 is a coarse grid used for the long-time wave dynamics after the bubble has vented.

Table 3 — Grid Parameters Used for the UMD 2-D Box Simulations

Grid	Time Interval	h (in.)	X_R (in.)	Z_B (in.)	Z_T (in.)	$N_x \times N_z$
1	$0.0 \le t \le 0.00025$	0.0012	0.6	–4.3	–3.1	70×150
2	$0.00025 \le t \le 0.2$	0.012	9.0	–8.4	8.4	76×184
3	$0.2 \le t \le 1.5$	0.024	9.0	–8.4	8.4	38×97

Figure 14 shows a simulation of the UMD 2-D box experiment using the model described in this report. For this computation, the yield stress (nondimensionalized by dividing by the ambient pressure) was $\hat{\tau} = 0.59$. For these simulations, the ratio of yield stress to plastic viscosity was $\hat{\tau}/\mu_0 = 83$. The parameter $\alpha = 10$ was used in the Papanastasiou model Eq. (36). The early expansion of the bubble, jet formation and collapse appear to be reasonably well predicted. However, the effect of the jet impact on the bottom of the channel is much more severe in the model than in the experiment. Furthermore, the model is not able to predict the washback or sedimentation of the sand back into the channel. The final (steady-state) channel ($t \ge 1.0$) is substantially deeper than either the apparent or true craters formed from the experiment. Also, the "lip" (area of raised sand at the channel edges) is higher and narrower than in the experiment.

Figure 15 shows a simulation of the same experiment but with a scaled yield stress of $\hat{\tau} = 0.059$. In this case, the steady-state channel is in reasonably good agreement with the experimental channel. Unfortunately, when comparing Fig. 13 to Fig 15, one sees little resemblance of the dynamics from the simulation to the experiment. With the lower yield stress, the bubble jets at a much later time than in the experiment. Also, the simulation shows the bubble migrating below the initial charge location. There is no evidence of this in the images from the experiment. This example clearly shows the danger in simply comparing the final results of a simulation to an experiment, particularly when "violent" nonlinear hydrodynamics is occurring.

Figure 16 compares the final channels from the experiment and simulations using various yield stresses. It is evident that none of the simulations are capable of providing an accurate description of the final channel profile. With increasing yield stresses, the depth of the channel approaches that of the experiment. However, the width of the channel also decreases and becomes less like the experiment.

Based on Fig. 16, the current model does not appear to be capable of reliably predicting the complex interaction between the sand and water upon the bubble jet collapse or the later sedimentation of the sand back into the channel. However, the early time bubble formation can be accurately predicted. In another experiment in the UMD 2-D box, in which $H_w = 3.0$ in. and $D_b = 0.6$ in., the outline of the bubble at its maximum volume was clearly displayed in the video image. This image was compared to simulations using various yield stresses in Fig. 17. In this figure, the agreement of the simulation with $\hat{\tau} = 0.295$ to the experiment is remarkable. In the case of no yield stress (here the saturated sand is treated as a dense incompressible liquid), the bubble has an oval shape and is much deeper in the sand than the experiment indicates. Incorporating a yield stress produces more realistic bubble profiles in which the bubble radius is larger in the water region than the sand. This is intuitively correct and verified by the image from the experiment in Fig. 17.

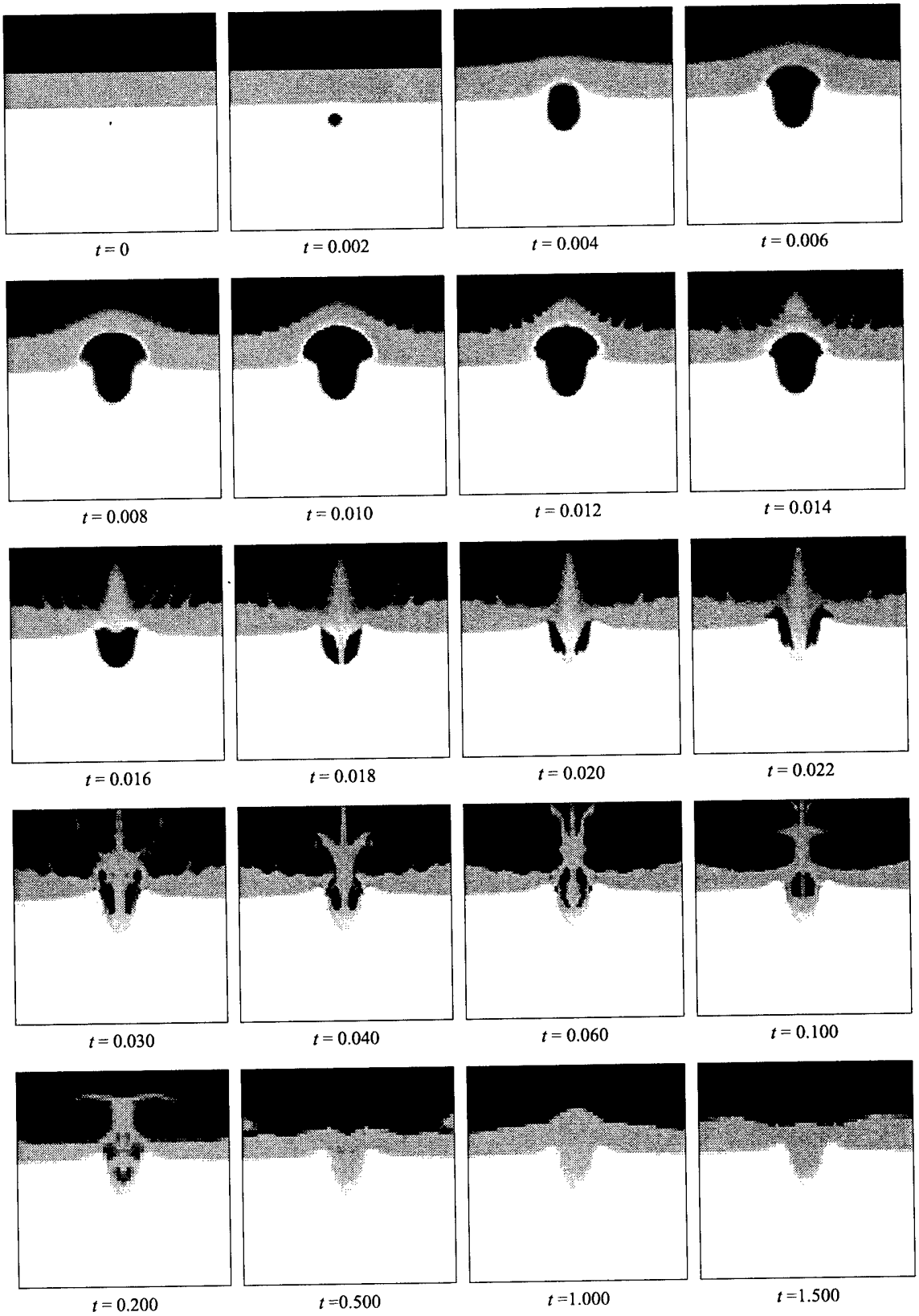

Fig. 14 — Simulation of the UMD 2-D box experiment $H_w = 2.5$ in., and $D_b = 1.0$ in. using $\hat{\tau} = 0.590$

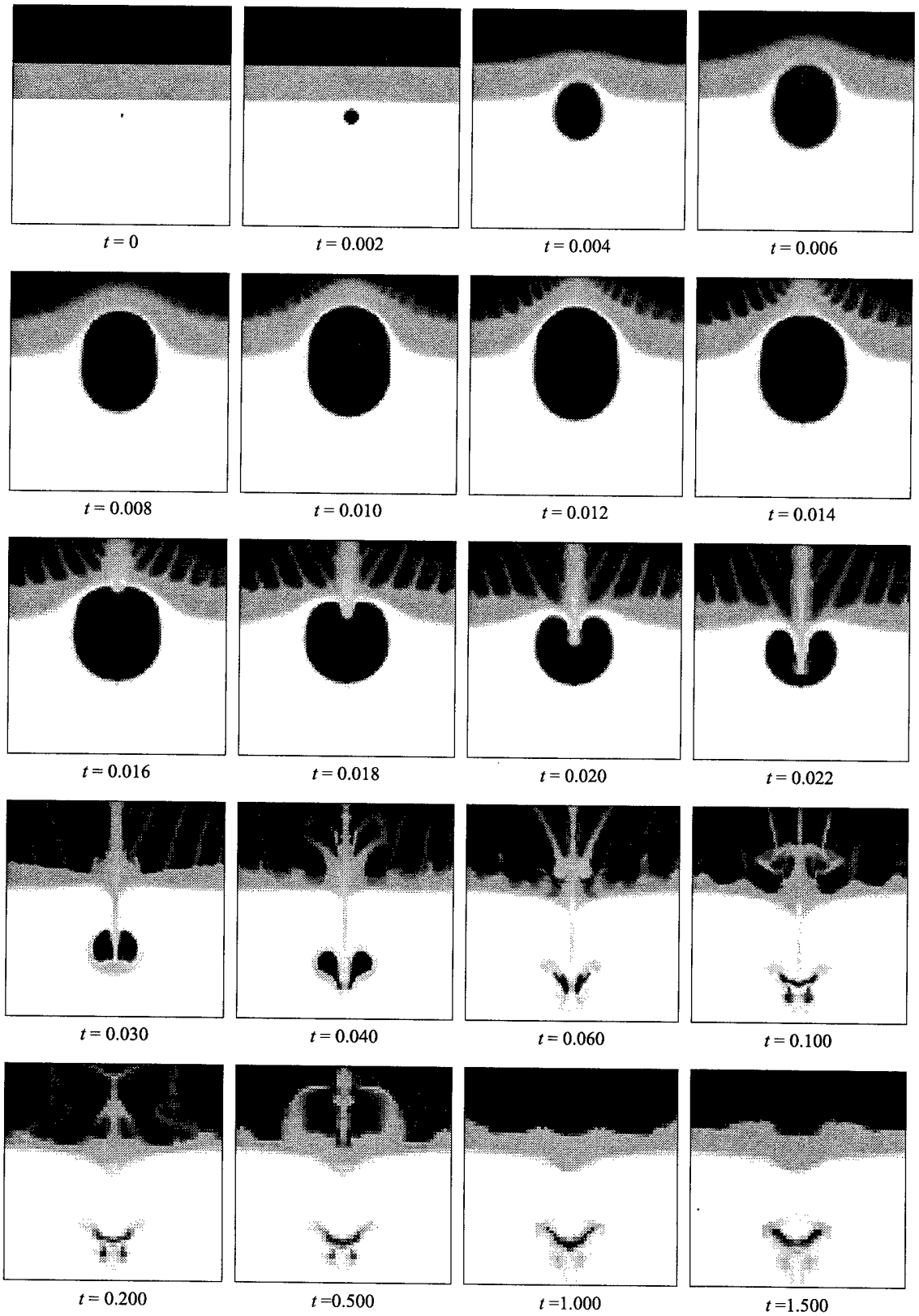

Fig. 15 — Simulation of the UMD 2-D box experiment $H_w = 2.5$ in., and $D_b = 1.0$ in. using $\hat{\tau} = 0.059$

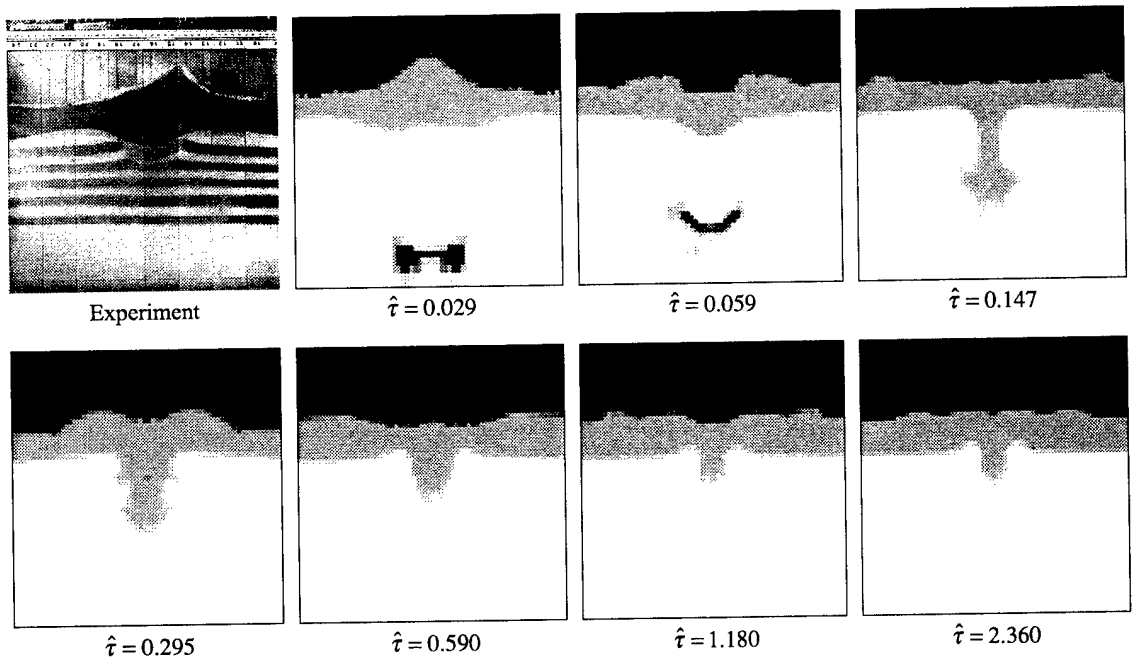

Fig. 16 — Comparison of final channel from experiment and computations with different yield stresses

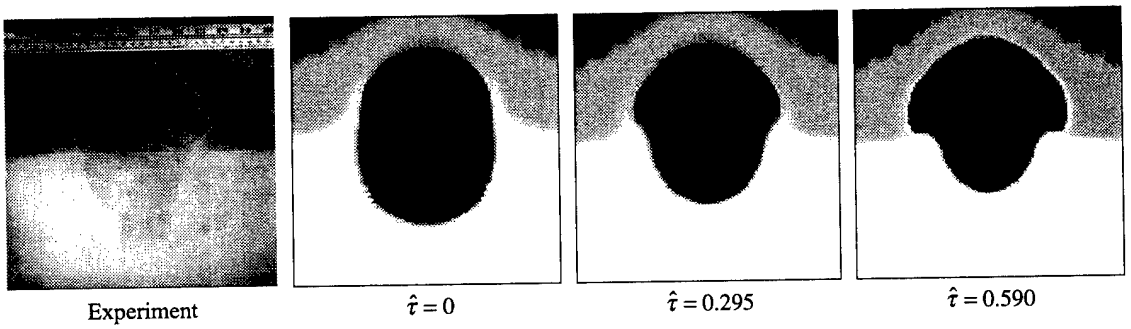

Fig. 17 — Comparison of bubble at maximum volume for the case $H_w = 3.0$ in. and $D_b = 0.6$ in.

SUMMARY AND CONCLUSIONS

In an attempt to model explosive channeling in water-covered sand, we have generalized a model which has been successful for violent free-surface motions with a single incompressible liquid species. The new model included viscoplastic forces for saturated sand, so that nontrivial steady-state conditions (e.g., channels) could be predicted. Due to the stiff nature of the equations employed to approximate a Bingham plastic, a fully implicit numerical treatment was required for stability. The model was successfully tested on a benchmark problem of slug flow in a circular cylinder, for which the exact solution is known. It was also tested on a problem of a free-standing cylinder of material under the influence of gravity, which qualitatively demonstrated the capability to predict nontrivial steady-state deformations.

For simulations of channeling, the early time bubble expansion and first collapse were accurately predicted, provided that an appropriate value for the yield stress was used. This result is encouraging and suggests that the Bingham model is appropriate, at least during the first period of the bubble dynamics. The effect of the water jet impacting the bottom of the channel appeared to be overpredicted in the

simulations. Also, no mechanism for the sedimentation or the wash back of the sand refilling the channel is provided in the model. This wash back is responsible for the substantial difference observed between the apparent and true channels.

So far, we have considered the treatment of multiple species with only one flow field representing the velocity of the mixture of the species. This formulation does not model the flow of water through the sand, which can influence the sand strength and describe the settling of sand mixed with water. In future work, we will describe a model that includes a separate velocity field for each species. This model will also account for the porosity of sand, by constraining its volume fraction to be bounded by a quantity less than unity. The permeability of sand can be modeled by the inclusion of drag terms in the momentum equations. Finally, more physically realistic stress models for the saturated sand, such as those satisfying the Mohr-Columb criterion [19-21] or Prager-Drucker condition [22, 23] will be examined.

ACKNOWLEDGMENTS

This work was supported through the Office of Naval Research (ONR) through the office of Dr. Thomas Swean (Code 3210E). This research was part of the Mine Countermeasures 6.2 Block managed by Leslie C. Taylor of the Naval Surface Warfare Center, Indian Head Division (NSWC-IH). We also thank our collaborators from the University of Maryland, Aerospace Engineering Department; namely, Prof. William Fourney, Dr. Richard Dick, Zeyad S. Abu-Hassanein, Oliver Oberle, and Uli Leiste for conducting the experiments and providing the images from the UMD 2-D box experiments.

REFERENCES

1. Naval Surface Warfare Center, Indian Head Division, Indian Head, Md., IHTR 1924, "Explosive Cratering and Channeling of Shallow Water Bottoms," D. Nell, D. Betancourt, and S. Van Denk, 1999.

2. W.L. Fourney, R. Randles, and R. Dick, "Displacement of Sand and Obstacles Under Standing Water with Explosives," *FRAGBLAST—Int. J. Blast. Fragm.* **1**, 393-416 (1997).

3. R.H. Cole, *Underwater Explosions* (Princeton University Press, Princeton, 1948) Ch. 8, pp. 270-353.

4. J.R. Blake and D.C. Gibson, "Growth and Collapse of a Vapour Cavity Near a Free Surface," *J. Fluid Mech.* **111**, 99-123 (1981).

5. Naval Surface Warfare Center, Dahlgren Division, Dahlgren, Va., NSWCDD/TR-94/156, "Computations and Experiments of Shallow Depth Explosion Plumes," W.G. Szymczak and J.M. Solomon, 1996.

6. W.G. Szymczak and C.E. Higdon,"Model Validations and Predictions for Water Barrier Defense," NRL/FR/7130--98-9880, Naval Research Laboratory, Washington, D.C., 1998.

7. G.A. Young, "Dispersion of the Chemical Products of Underwater Explosions," NSWC TR 82-404, Naval Surface Weapons Center Technical Report, Silver Spring, Md., 1984.

8. Naval Surface Warfare Center, Indian Head Division, Indian Head, Md., IHTR 2188, "Spring 1998 Explosive Testing at Port Wakefield, Australia Including Explosive Cratering and Channeling," L.C. Taylor, W.L. Fourney, and D. Robeson, 1999.

9. Naval Surface Warfare Center, Dahlgren Division, Coastal Systems Station, Panama City, Fla., "Video of Explosions from Eglin AFB," J. Luturco, 1997.

10. J.C.W. Rogers, "Incompressible Flows as a System of Conservation Laws with a Constraint," *Seminaries IRIA Analyse Contrôle de Systèmes*, 141-162 (1978).

11. J.C.W. Rogers, W.G. Szymczak, A.E. Berger, and J.M. Solomon, "Numerical Solution of Hydrodynamic Free Boundary Problems," in *Free Boundary Problems, International Series of Numerical Mathematics,* (Birkhäuser Publishing Ltd., Basel, Switzerland, 1990), **95**, pp. 241-266; Proceedings of the Conference on Free Boundary Problems—Numerical Methods and Optimal Control, K.-H. Hoffmann and J. Sprekels, eds., July 9-19, 1989, Oberwolfach, Germany.

12. J.C.W. Rogers and W.G. Szymczak, "Computations of Violent Surface Motions: Comparisons with Theory and Experiment," *Phil. Trans. R. Soc. Lond.* **355**(A), 649-663 (1997).

13. W.G. Szymczak, J.C.W. Rogers, J.M. Solomon, and A.E. Berger, "A Numerical Algorithm for Hydrodynamic Free Boundary Problems," *J. Comp. Phys.* **106**, 319-336 (1993).

14. C.W. Hirt and B.D. Nichols, "Volume of Fluid (VOF) Method for the Dynamics of Free Boundaries," *J. Comput. Phys.* **39**, 201-225 (1981).

15. D.E. Kothe and R.C. Mjolsness, "RIPPLE: A New Model for Incompressible Flows with Free Surfaces," *AIAA J.* **30**, 2694-2700 (1992).

16. V.G. Kozlov, A.A. Ivanova, and P. Evesque, "Sand Behavior in a Cavity with Incompressible Liquid under Vertical Vibrations," *Europhys. Lett.* **42**(4), 413-418 (1998).

17. A. Lange, M. Schröter, M.A.Scherer, A. Engel, and I. Rehberg, "Fingering Instability in a Water-Sand Mixture," *Eur. Phys. J. B*, **4**, 475-484 (1998).

18. B. Singh, T.G. Callcott, and G.R. Rigby, "Flow of Fluidized Solids and Other Fluids in Open Channels," *Powder Techn.* **20**, 99-113 (1978).

19. M.A Goodman and S.C. Cowin, "Two Problems in the Gravity Flow of Granular Materials," *J. Fluid Mech.*, **45**(2), 321-339 (1971).

20. D.F. McTigue, "A Nonlinear Constitutive Model for Granular Materials: Application to Gravity Flow," *J. App. Mech.*, **49**, 291-296 (1982).

21. S.B. Savage, "Gravity Flow of Cohesionless Granular Materials in Chutes and Channels," *J. Fluid Mech.*, **92**(1), 53-96 (1979).

22. M.A. Diez and L.A. Godoy, "Viscoplastic Incompressible Flow Of Frictional-Cohesive Solids," *Int. J. Mech. Sci.* **34**(5), 395-408 (1992).

23. S.A. Elaskar and L.A. Godoy, "Constitutive Relations for Compressible Granular Materials using Non-Newtonian Fluid Mechanics," *Int. J. Mech. Sci.* **40**(10), 1001-1018 (1998).

24. R.B. Bird, W.E. Stewart, and W.N. Lightfoot, *Transport Phenomena* (John Wiley & Sons, Inc., New York, 1960).

25. R.B. Bird, R.C. Armstrong, and O. Hassager, *Dynamics of Polymeric Liquids, Volume 1 Fluid Mechanics* (John Wiley & Sons, Inc., New York, 1987).

26. T.R.H. Davies, "Large Debris Flows: A Macro-Viscous Phenomenon," *Acta Math.* **63**, 161-178 (1986).

27. J.G. Oldroyd, "A Rational Formulation of the Equations of Plastic Flow for a Bingham Solid," *Proc. Cambr. Phil. Soc.* **43**, 100-105 (1947).

28. T.C. Papanastasiou, and A.G. Boudouvis, "Flows of Viscoplastic Materials: Models and Computations," *Comput. and Structures* **64**, 677-694 (1997).

29. R. Darby, "Hydrodynamics of Slurries and Suspensions," in *Encyclopedia of Fluid Mechanics, Vol 5, Slurry and Suspension Flow Properties*, N.P. Cheremisinoff ed. (Gulf Publishing Co., Houston, 1986), pp. 49-91.

30. L.I. Rudin, S. Osher, and E. Fatemi, "Nonlinear Total Variation Based Noise Removal Algorithms," *Physica D* **60**, pp. 259-269 (1992).

31. W.K. Pratt, *Digital Image Processing* (John Wiley & Sons, New York, 1991).

32. H.G. Snay, J.F. Goertner, and R.S. Price, "Small Scale Experiments to Determine Migration of Explosion Gas Globes Towards Submarines," NAVORD Report 2280, Naval Ordnance Laboratory, Silver Spring, Md., 1952.

33. W.L. Fourney, D.J. Goodings, R.J. Bonenberger, and U. Leiste, "Mechanisms of Cratering in Water Covered Soils," submitted to *FRAGBLAST—Int. J. Blasting and Fragmentation.*